THE UNIVERSITY OF CHICAGO

ON THE POPULATION II DISTANCE SCALE: THE TIP OF THE RED GIANT BRANCH DISTANCES TO LOCAL GALAXIES

A DISSERTATION SUBMITTED TO
THE FACULTY OF THE DIVISION OF THE PHYSICAL SCIENCES
IN CANDIDACY FOR THE DEGREE OF
DOCTOR OF PHILOSOPHY

DEPARTMENT OF ASTRONOMY AND ASTROPHYSICS

BY

DYLAN T. HATT

CHICAGO, ILLINOIS

AUGUST 2017

Copyright © 2017 by Dylan T. Hatt

All Rights Reserved

Dedicated to my parents, Martha & Daniel Hatt

TABLE OF CONTENTS

LIST OF FIGURES

ACKNOWLEDGMENTS

Several individuals have made this work possible. I thank my advisors, Richard Kron and Wendy Freedman, for the many years of advice and support. I also thank Wendy Freedman and Barry Madore for the opportunity to contribute to their *HST* program. I further thank many of the collaborators who have given feedback and guidance on my research projects, including Rachael Beaton, Victoria Scowcroft, Mark Seibert, and Taylor Hoyt, among others. This work has made extensive use of the DAOPHOT astronomical software, which is developed and maintained by Peter B. Stetson, who has also given direction on its usage.

ABSTRACT

The difference between direct and indirect measures of H_0, i.e. via SNe Ia distances anchored by Cepheids and via modeling of the Cosmic Microwave Background, stands at an average $> 3\sigma$. This tension has motivated a second look at the calibration of the extragalactic distance scale. Population II stars have gained favor as an independent calibrator of SNe Ia, bypassing the possible systematics associated with the traditional Cepheid-based distances. We present high-fidelity distances to four local galaxies—IC 1613, NGC 4424, NGC 4526, and NGC 4536—using the Tip of the Red Giant Branch, which is a prominent observable that is defined by well-understood stellar astrophysics. We further compare these results with existing Cepheid-based distances and demonstrate a good correspondence between distances derived from stars of Population I and II on a galaxy-by-galaxy basis.

CHAPTER 1

INTRODUCTION

1.1 A Cosmological Conundrum

The value of current expansion rate of the Universe (H_0) holds importance in the field of cosmology because it is highly co-variant with other cosmological parameters. Specifically, a precision of better than 1% would be required to break the degeneracy between itself and others [see discussion in 46]. The present $> 3\sigma$ difference in the average estimates of H_0 from different methodologies is therefore a potential cause for concern (see Figure 1.1). Should this tension persist, it could necessitate non-standard physics in the early or late Universe [3] or a re-working of the established extragalactic distance scale [2].

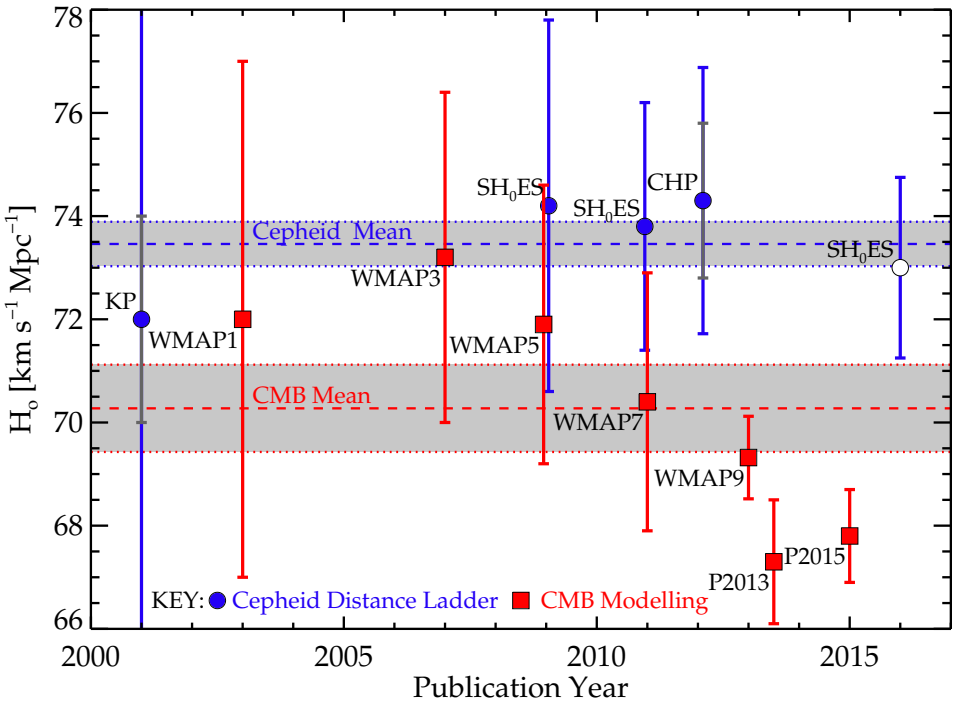

Figure 1.1: Compilation of direct and indirect measures of H_0 via [2].

These resolutions stem from the two methodologies employed in the determination of H_0, namely a indirect measure based on modeling of the Cosmic Microwave Background under

ΛCDM [29, 47], and a direct measure based on the distances to Type Ia Supernovae (SNe Ia) [most recently 17, 50], which are calibrated in the local Universe via classical Cepheids (henceforth, simply referred to as 'Cepheids'). The focus of this work in on the latter methodology, i.e. we undertake a re-calibration the SNe Ia distance scale using Population II (Pop II) stars, whose use as standard candles is completely independent of Cepheids. In the following sections, we discuss the possible systematics associated with Cepheids and their resolution through use of Pop II stars.

1.2 Reconsidering the Cepheid-based distance scale

Cepheids are an established tool for the extragalactic distance scale, but questions remain about their reliability given their intrinsic placement in the dusty components of galaxies (see Figure 1.2). The first possible systematic in their distance determinations arises from the fact that said dust contributes an unknown amount of reddening internal to the parent galaxy. It is possible to reduce the impact of reddening by applying knowledge of the observed relative colors of stars when multi-band photometry is available [see definition of Wesenheit functions in 32]. Conceptually, these converted magnitudes will be identical to those when no reddening is present. This approach assumes a reddening law for the parent galaxy, however, which itself is an unknown and therefore an additional source of uncertainty.

To further reduce the impact of reddening, which can also include foreground extinction in the Milky Way, it is common to shift observations to longer wavelengths such as the near-infrared (NIR). For Cepheids, however, this introduces a new possible systematic. Cepheids are most luminous in the optical whereas other populations like Red Giant Branch (RGB) stars are brighter in the NIR. Thus while Cepheids are visually prominent at shorter wavelengths, a sea of RGB stars emerges in the NIR that directly impacts photometric accuracy. Without high-resolution imaging and an extended observing program to confirm light curve structure, it cannot be verified that a Cepheid has been properly identified and measured.

A further systematic is the uncertainty in the metallicity dependence of their period-

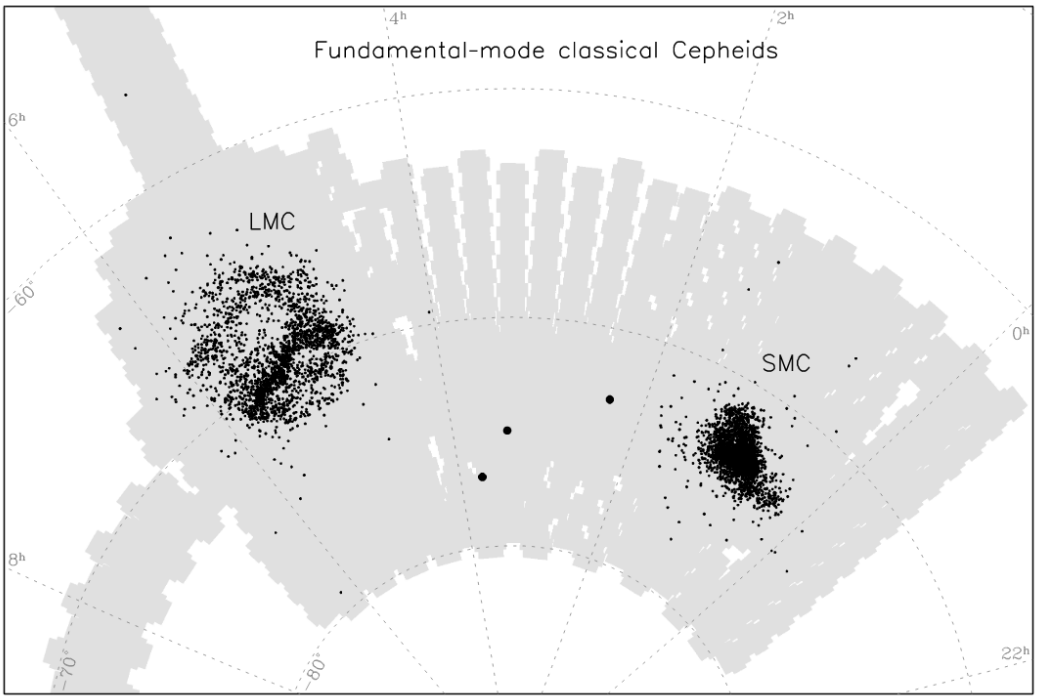

Figure 1.2: Cepheids trace dusty features of galaxies, e.g. classical Cepheids in the Large and Small Magellanic Clouds via [63].

luminosity (PL) relations. The overall impact of metallicity is debated, and but there is general consensus that the slope of the PL relations is insensitive to metallicity. On the other hand, a trend in the zero-point with metallicity has been noted in observation [34] and theory [5], with a lessening impact in the NIR. More recent studies have spotted a metallicity trend in the NIR [59], however, which indicates that the full effect on the zero-point is not yet known.

Should theoretical and observational progress be made on the metallicity dependence of Cepheid PL relations, it will remain a challenge in at least the near-term to assess the metal content of more distant galaxies. The modified form of the PL relation, the period-Wesenheit (PW) relation (discussed again later in this work), is predicted to have vanishing metallicity effects [5]. This independence relies on accurate knowledge of the passband-specific metallicity-dependence, however, which is not only currently uncertain but relies primarily on only two local sources for calibration, namely the Large and Small Magellanic Clouds (LMC, SMC).

These systematics—reddening, source crowding, and metallicity—are considered 'known'. It is plausible that further systematics exist that are 'unknown'. For example, the fact that Cepheids are limited to spiral galaxies is an indication of a biased sample, though the extent of this bias has not been quantified. To assess the impact of systematics on Cepheid-based distances, it is critical to provide an independent check beyond the few instances where non-Cepheid distances are known to high precision, e.g. the eclipsing binary distances to the LMC/SMC [45, 23] and M 31 [49, 64], as well as the maser distance to NGC 4258 [22, 24]. In the following section, we discuss the use of Pop II stars as an independent distance indicator that bypasses the known and possible unknown systematics associated with Cepheids.

1.3 An Independent Route to H_0 using Population II stars

The intrinsic properties of Pop II stars and their distribution within galaxies alleviate all of the aforementioned possible systematics in Cepheid-based distances. On the topic of internal extinction to due to dust in the host galaxy, Pop II stars populate the halos of galaxies, which are virtually dust-free. Furthermore, any remaining extinction (possibly in the foreground) can be reduced by observing in the NIR. Whereas this switch to longer wavelengths introduced crowding effects for Cepheids, the halos of galaxies are fortuitously intrinsically low in their surface density of stars.

On the topic of metallicity, Pop II stars are by definition old (> 10 Gyr) and metal-poor, with a typical metallicity range of $10^{-4} < Z < 10^{-3}$. This property reduces, if not eliminates, the influence of metallicity on the distance scale zero-point calibration. Beyond the known, possible systematics associated with Cepheids, Pop II stars are found in all galaxy types, thereby increasing the eligible number of SNe Ia calibrators. These fundamental properties make Pop II stars a promising tool for a fresh look at extragalactic distance scale.

Pop II stars are standard candles at several of their stages of evolution, including the Horizontal Branch (e.g. RR Lyrae), the Red Clump, and Globular Cluster Luminosity Functions. The most promising for the extragalactic distance scale, and the subject of this

work, is the Tip of the Red Giant Branch (TRGB), which is discussed in detail in the following sections.

1.4 Physical Origin of the Tip of the Red Giant Branch

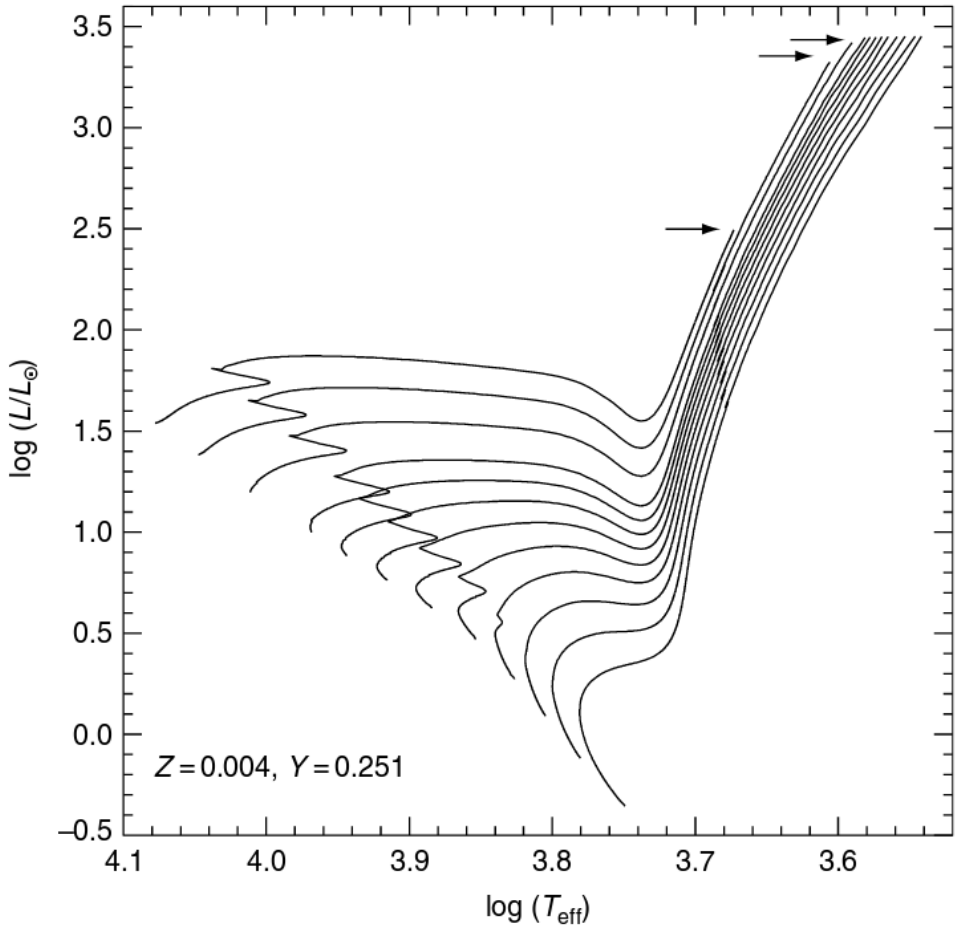

Figure 1.3: Low-mass stars achieve a near constant luminosity at the TRGB (Main-sequence and RGB evolution via [54]).

As low-mass ($\lesssim$ 1.8 $M_{\odot}$) stars ascend the RGB via hydrogen shell burning, helium ash accumulates onto the inert stellar core. Eventually, the helium core becomes electron-degenerate under immense gravitational pressure. The core continues to grow in mass until it reaches $\approx 0.48\ M_{\odot}$ (corresponding to $\sim 10^8$ K) when helium burning begins via the triple-α process. Due to the presence of the degeneracy, the star is unable to compensate for the

energy production through expansion. Instead, the energy is held internally, further fueling the highly temperature-sensitive helium burning. The core temperature rises precipitously until thermal pressure regains dominance and the degeneracy is lifted. At this point, stars stabilize into helium-core and hydrogen-shell burning Horizontal Branch or Red Clump stars (see Figure 1.3). Because of the degenerate core, this short-lived thermonuclear runaway process ignites at a well-defined critical core mass, which constrains the maximum stellar luminosity achievable for stars ascending the RGB. It follows that this abrupt phase of stellar evolution, i.e. when RGB stars reach the TRGB, is a standard candle.

1.5 Tip of the Red Giant Branch as a Distance Indicator

The advent of digital, wide-field, and space-based observations has greatly increased the usage of the TRGB as a galaxy distance indicator. Since of order 400 stars within the first magnitude of the RGB is needed for at least 1 TRGB star [33], nearby galaxies have typically needed a wider field-of-view to collect a large enough sample of RGB stars. For more distant galaxies, their halos were unresolved until the arrival of modern, high-resolution space-based observations like the Hubble Space Telescope (*HST*).

To date, the TRGB method has achieved remarkably precise measurements for Local Group galaxies, comparable to or even out-performing traditional methods like Cepheids. The method naturally has its own sources of uncertainty, however. A known systematic is the dependence of luminosity on metallicity for individual TRGB stars, where metal content within the stellar atmosphere shifts observed flux into the NIR. In the optical, this effect is observed as a redder, downward sloping TRGB. In the NIR, on the other hand, the trend is reversed. We note here that the fact that the metal-composition of stars manifests itself as prominent observable in color-magnitude space is an enormous advantage over Cepheids, whose shifting of a PL/PW zero-point due to metallicity is observationally indistinguishable from another in magnitude-$\log P$ space. Furthermore, the TRGB is a fixed, non-variable feature of galaxies and therefore requires far less observing time than Cepheids.

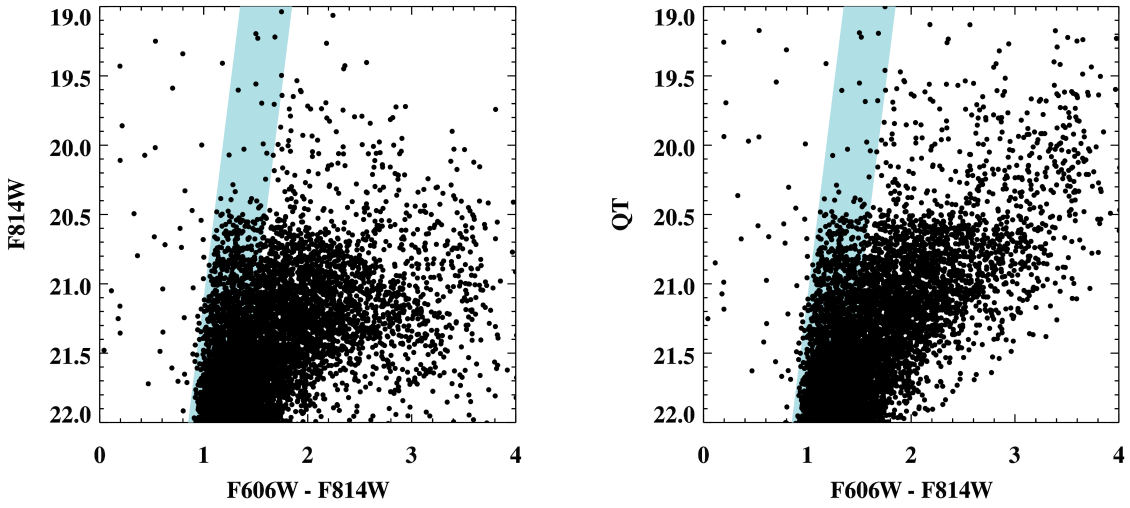

Figure 1.4: Sample M 31 CMD before (left) and after metallicity ('QT') correction (right) (Hatt et al. in prep). The metal poor component of the RGB (shaded blue) shows that the TRGB is a prominent enough to not necessitate a metallicity correction.

Given the amount of current literature on the TRGB and independent distance measurements to local galaxies, however, the TRGB of galaxies (especially their halos) have empirically well-calibrated slopes in color-magnitude space. In the cases where there is significant metal content, contemporary studies, e.g. [33] and [27], have developed tools to rectify the optical TRGB to the metal-poor spectrum. At the transition between the optical and infrared, approximately in the I-band, it follows that the slope of the TRGB is roughly flat, especially for the most metal-poor stars [see discussion in 54]. Historically, most studies, including this work, have leveraged knowledge of this transition point to craft observations of the TRGB. The luminosity of the TRGB in the I-band is remarkably fixed over a wide range of ages [11], including as metal-enriched as [Fe/H] ≤ -0.3 dex [1]. Observations of galaxies in the I-band, or counterparts such as *HST* F814W, therefore make the TRGB a remarkably well-defined observable. Figure 1.4 demonstrates the I-band TRGB for M 31 (Hatt et al. in prep). The metal-rich TRGB stars can be corrected to the metal-poor spectrum, but for this galaxy as an example, the metal-poor component is well-populated enough to demonstrate the flatness of the metal-poor I-band TRGB (shaded in blue).

A further systematic, and one that is unique to the TRGB, is the presence of thermally-pulsating asymptotic giant branch (TP-AGB, hereafter simply AGB) stars. These stars often populate the color-magnitude space parallel to and above the RGB [for an overview of this evolutionary phase, see 20, 8]. Nonetheless, this systematic is often minimized by observing the halos of galaxies, which are already ideal targets for the TRGB because of low source crowding and low internal reddening. Here, low-mass stars that ascend the asymptotic giant branch do not exceed the TRGB in brightness as greatly as intermediate mass stars [see low-mass evolution in Figure 4.2 of 8], and therefore effectively do not obscure the tip when a primarily low-mass halo population of stars is observed.

1.6 The Carnegie-Chicago Hubble Program

The Carnegie-Chicago Hubble Program (CCHP,[14]) aims to use Pop II stars, and in particular the TRGB, as an independent calibrator of SNe Ia, and hence an alternate and potentially more accurate route to H_0. As part of the program and relevant to the work presented here, we have obtained new, high-fidelity TRGB distances to several local galaxies—namely IC 1613, NGC 4424, NGC 4526, and NGC 4536—using observations from *HST* and, in the case of IC 1613, additional ground-based IMACS imaging using the Magellan-Baade Telescope. For each galaxy, we resolve their TRGBs to better than 0.05 mag precision and distances to better than 3%. Most of these galaxies also have existing Cepheid-based distances to serve as a comparison to the Pop II distance scale.

The first galaxy as part of this study is IC 1613, which is an ideal target for the study of both Pop I and II stars for several reasons. It is nearby at $\sim 730 - 770$ kpc [18, 4, 58], it is face-on, and it is known to have low source crowding. Additionally, the galaxy is metal-poor with its Pop II stars ranging between $-1.2 \leq$ [Fe/H] ≤ -1.6 dex depending on the method used [see e.g. 28, 61]. IC 1613 is also at a high Galactic latitude [38], with foreground line-of-sight reddening estimated to be $E(B-V) \leq 0.025$ [57, 56]. Moreover, the visibility of background galaxies through the body of the galaxy has been used as a signal that internal

reddening is negligible [55, 15]. Given the proximity of IC 1613, the analysis here also makes use of their RR Lyrae variables (which are several magnitudes fainter than the TRGB) as an internal consistency check on Pop II distances.

The remaining galaxies—NGC 4424, NGC 4526, and NGC 4536—are an equally valuable component of this work because they themselves are SNe Ia hosts and all lie at a comparable distance ~ 15 Mpc in the Virgo Constellation (also at a high Galactic latitude with $E(B - V) \leq 0.02$). For all but NGC 4526 there are also existing Cepheid-based distances, which will add to the comparison between Pop I and Pop II distance scales. The inclusion of these galaxies also allows for a comparison between near and far TRGB distances, demonstrating its reliability as a standard candle.

CHAPTER 2

OBSERVATIONS

Detailed observation summaries for the results presented in this work are given in [21] and Hatt et al. (in prep), Table 1 and Figure 1 of each respective work. In the following, we summarize the observation coverage and strategy.

For all observations as part of the CCHP, the exposure time calculations were intended achieve a signal-to-noise ratio of 10 at the anticipated magnitude of the TRGB. Each galaxy makes use of *HST* imaging from the Space Telescope Science Institute. For observations taken with the Advanced Camera for Surveys (ACS), we used FLC image products, which, beyond flat-field and bias corrections, also account for the detector's degradation in Charge Transfer Efficiency (CTE). For observations taken with the Wide Field Camera 3 (WFC3), we used the FLT image products. These are prepared in the same fashion as the FLC images sans the CTE-correction. In the case of IC 1613, additional ground-based observations were taken with the IMACS camera using the Magellan-Baade telescope, described below.

2.1 IC 1613

2.1.1 Archival HST *ACS/WFC*

We first made use of archival *HST* imaging of IC 1613 taken as part of the *Local Cosmology from Isolated Dwarfs* program [19]. A single field was imaged over 24 orbits between August 28 and 30, 2006, roughly $5'$ west of the galaxy center using the ACS/WFC instrument. A detailed log of observations is given in [4, their Table 1]. Figure 2.1 displays this pointing as alternating blue and red boxes at the center of the field-of-view. These observations served two purposes in this study: a calibration of ground-based IMACS imaging, described below, and the determination of RR Lyrae distances as an independent check on the TRGB distance to IC 1613.

2.1.2 CCHP WFC3/IR

We obtained near-infrared (F160W) imaging over 24 orbits between December 17 and 18, 2014, using the *HST* WFC3/IR instrument [PID:GO13691, PI: Freedman; 14]. These observations were specifically designed to provide well-sampled light curves for RRL. The orbits were divided between two overlapping WFC3/IR pointings in order to span the archival ACS/WFC field-of-view. The WFC3/IR imaging is shown relative to the wide-field IMACS and archival *HST* imaging in Figure 2.1 as solid black boxes at the center of the field-of-view, with the two pointings labeled 1 and 2.

2.1.3 CCHP HST *ACS/WFC*

In parallel with the observations described in the previous section were 24 orbits with the ACS/WFC instrument [PID:GO13691, PI: Freedman; 14]. The *HST* roll angle was set so that the pointings would occur at a larger projected separation from the center of IC 1613 to target halo RGB stars. This strategy resulted in a set of two pointings northwest of the galaxy center, which are shown relative to the wide-field IMACS imaging in Figure 2.1 as alternating gold and red boxes. The two pointings in the F606W and F814W filters are again labeled 1 and 2.

2.1.4 CCHP Baade-Magellan IMACS

Additional observations of IC 1613 were obtained on June 12, 2015, using the *Inamori-Magellan Areal Camera and Spectrograph* on the 6.5 m Magellan-Baade telescope at Las Campanas Observatory [12, IMACS]. We used the f/4 imaging mode to obtain a $15.46' \times 15.46'$ field-of-view in the BVI filters. The observations were centered on archival *HST* ACS/WFC imaging [4] in order to obtain a large sample of RGB stars well out into the surrounding halo.

Image processing was undertaken for each chip individually using standard procedures,

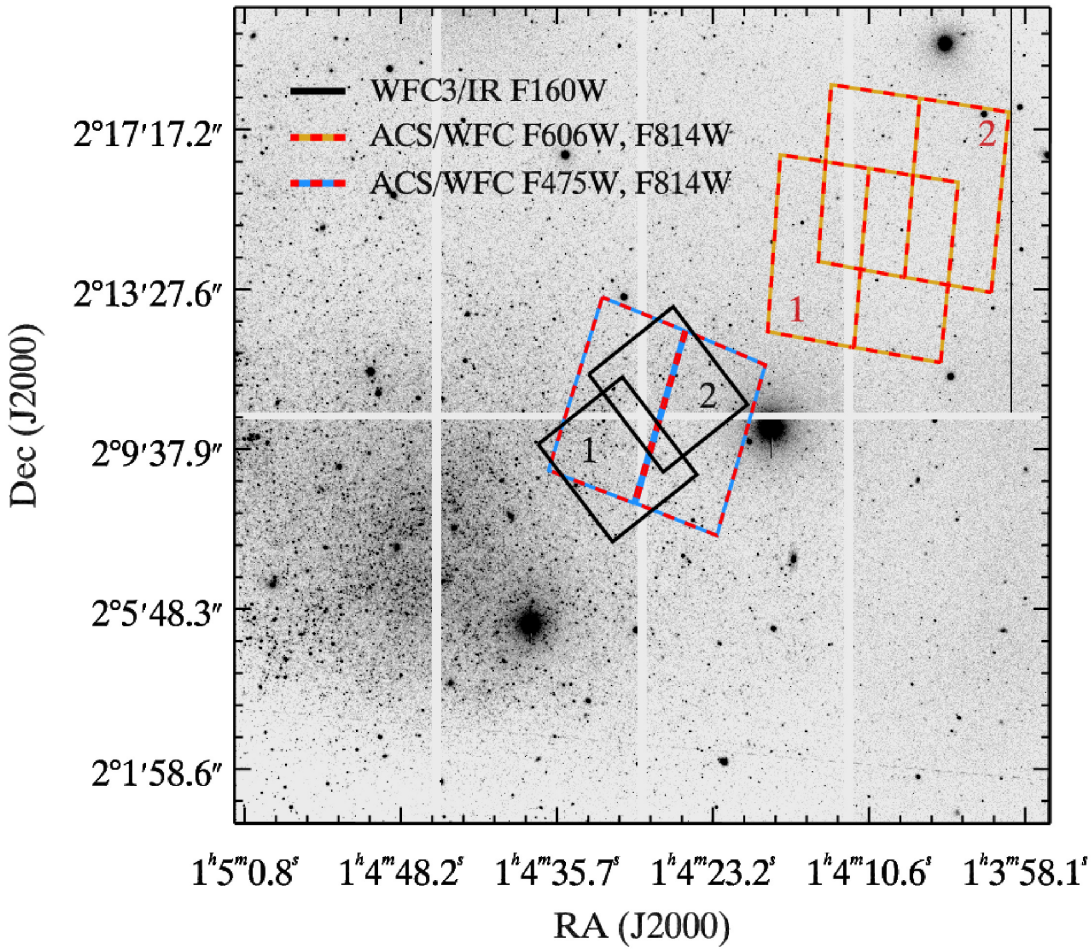

Figure 2.1: Magellan-Baade IMACS and *HST* imaging of dwarf galaxy IC 1613 [see 21]

including bias and per-filter flat-field corrections. The resulting chips were combined into a single image mosaic shown as the backdrop in Figure 2.1.

2.2 NGC 4424, NGC 4526, and NGC 4536

Observations for NGC 4424, NGC 4526, and NGC 4536 were taken over 6 orbits each between May 15, 2015, and December 15, 2015, using the *HST* ACS/WFC instrument. The selection of the fields is described in [2]. In summary, these fields were chosen to: i) avoid disks as

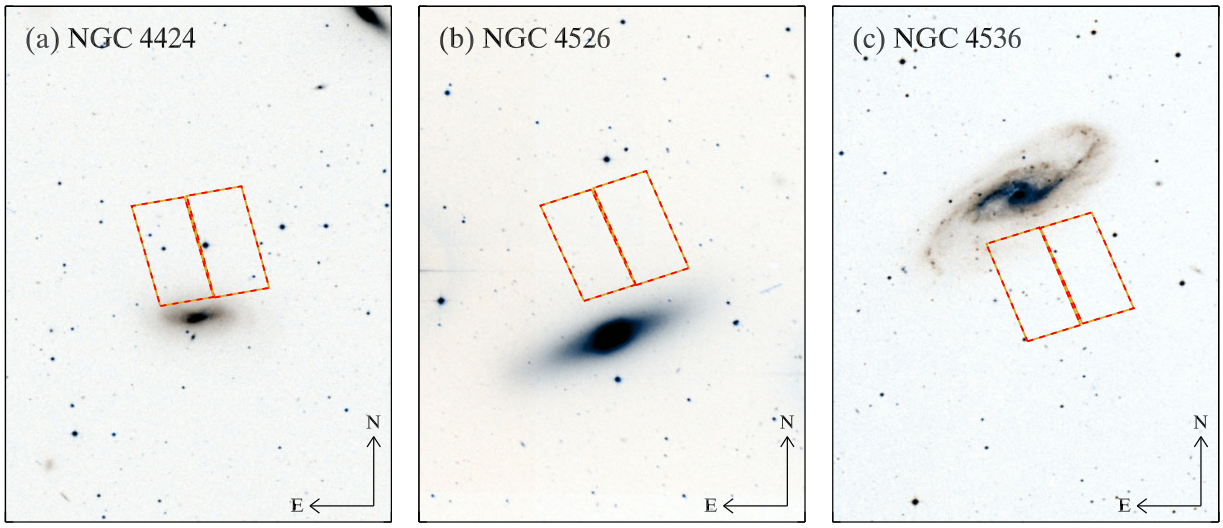

Figure 2.2: *HST* imaging of NGC 4424, NGC 4526, and NGC 4536 (Hatt et al. in prep)

well as young or tidal structures; ii) lie between the WISE W1 25-26 mag and the GALEX NUV 27-28 mag isophotes (where available); and iii) align along minor axes to maximize the number of halo stars within each field-of-view. Figure 2.2 displays the imaging coverage of the observations, taken in the F606W and F814W filters, where the backdrops are inverted-color DSS images.

2.3 Photometry

The approach to photometry is identical for all imaging datasets and is described in detail in [21], their Sections 2.1 and 2.2. Calibration parameters that are potentially unique to independent data reduction efforts, such as the difference in magnitude between the modeled and true PSF (aperture correction), are listed in [21] and Hatt et al. (in prep). In the remainder of this section we describe the salient features of the resulting color-magnitude diagrams (CMDs) for each galaxy.

Figure 2.3 displays the IC 1613 CMD using IMACS photometry. The ACS label indicates that the ground-based photometry was brought onto the *HST* flight magnitude system. Figure 2.3a is the complete sample of IMACS VI photometry centered on the core of IC 1613

and denoted by $r > 0$. Figure 2.3b is the same as the previous panel but using IMACS BI. Figure 2.3c displays the IMACS VI photometry greater than twice the half-light radius, or $r > 2r_h$, and Figure 2.3d is same as the previous panel but using IMACS BI. The entire photometric catalog of IC 1613 shows many stellar populations, such as two distinct blue plumes near $(V-I)_{ACS} \sim -0.5$ and red supergiants near $(V-I)_{ACS} \sim 0.7$ between $18 \lesssim I_{ACS} \lesssim 20$. On the other hand, the halo is composed of nearly exclusively RGB stars as well as some AGB stars brighter than the TRGB. An arrow in Figure 2.3d visually marks the location of the TRGB.

Figure 2.4a displays the CMD of NGC 4424. This field has the second most notable AGB/blended RGB component of the three galaxies as part of this study, although the TRGB is plainly visible by eye. This feature is possibly attributable in part to the relative proximity of the observations to the galaxy. Figure 2.4b is the CMD of NGC 4526, which has the most populated RGB of the Virgo Constellation galaxies, and consequently, the most populated TRGB. The lack of a substantial AGB/blended RGB component is also plainly visible. The primary contribution to the uncertainty in measuring the TRGB will therefore likely be photometric errors.

Finally, Figure 2.4c shows the CMD of NGC 4536, which has the most prominent AGB/blended RGB component of the three galaxies that are part of this study. Although the TRGB of NGC 4536 can be difficult to pinpoint visually depending on the visualization of the CMD, as with the other two galaxies, the jump in star count in the luminosity function due to the TRGB will be readily detected in later sections of this work.

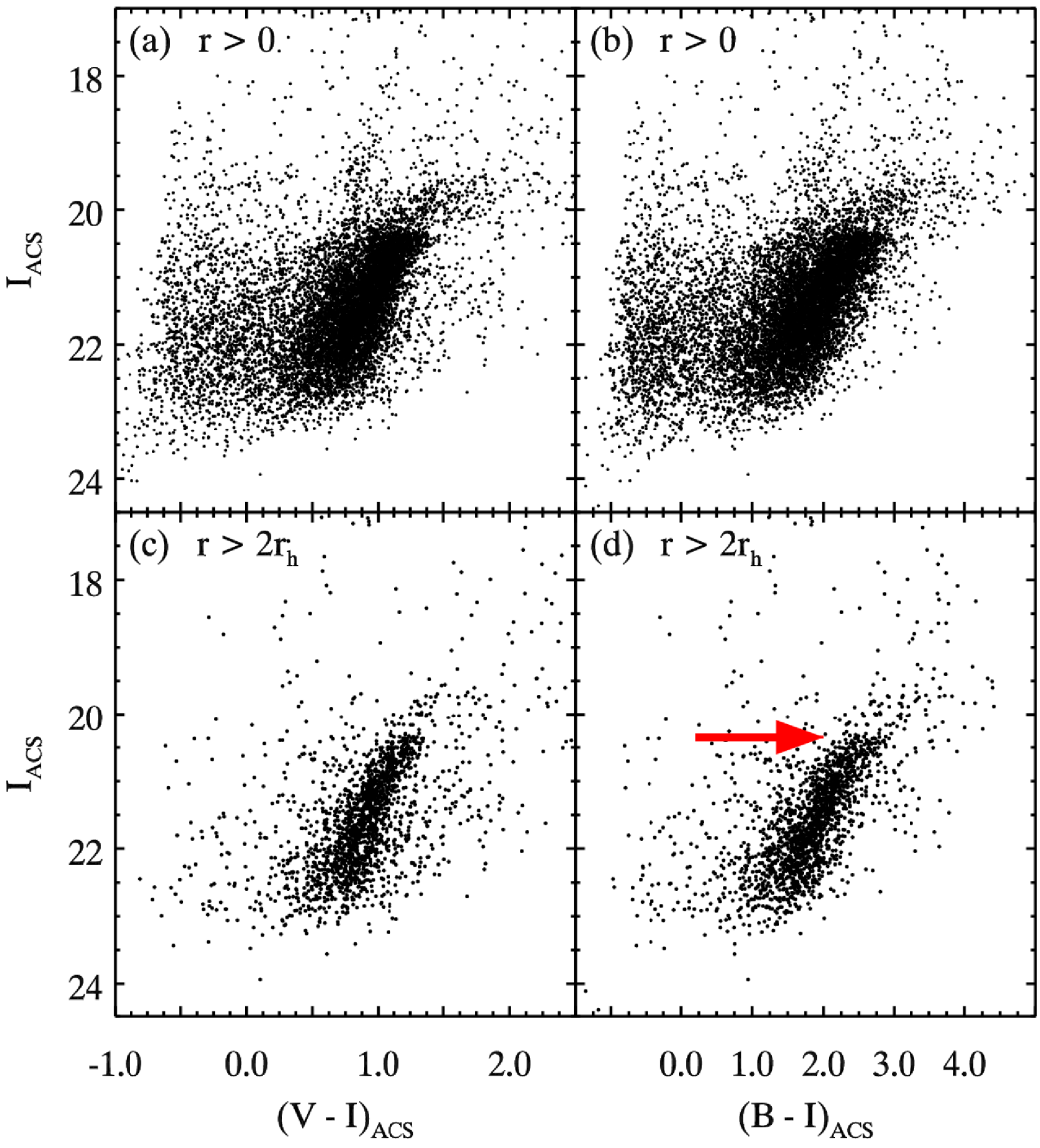

Figure 2.3: IC 1613 *BVI* CMDs using the IMACS camera on the Magellan-Baade telescope.

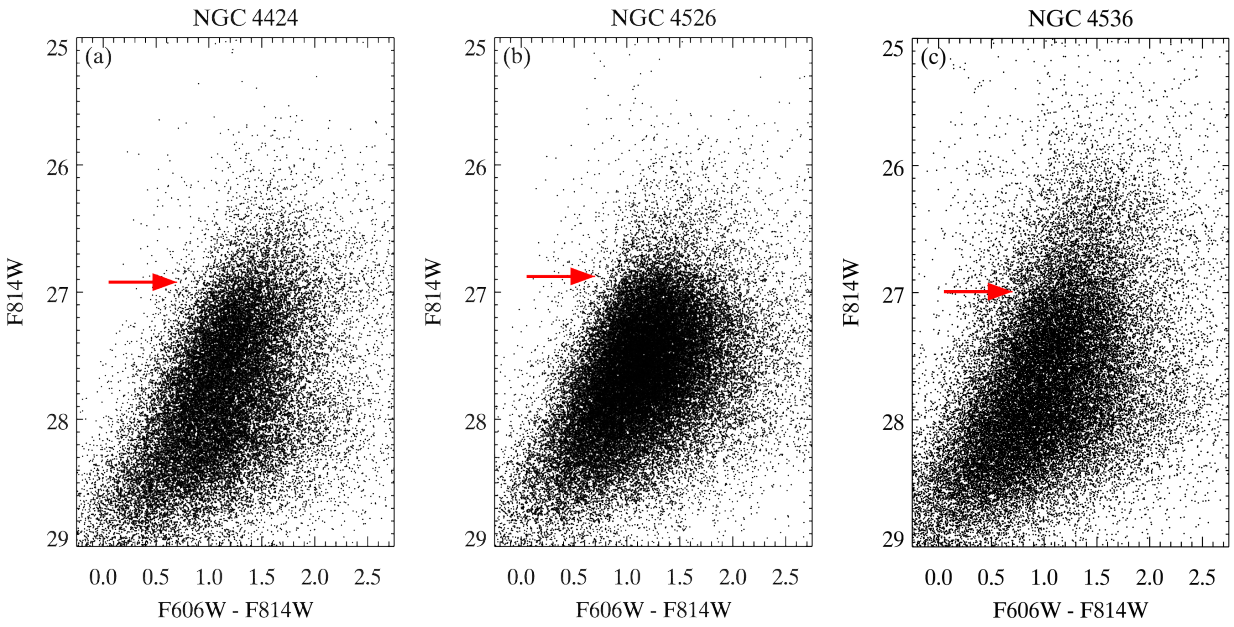

Figure 2.4: Color-magnitude diagrams of NGC 4424, NGC 4526, and NGC 4536

CHAPTER 3

THE TIP OF THE RED GIANT BRANCH

3.1 Introduction

As described previously, the TRGB is marked by a discontinuity in the stellar luminosity function (LF) of the RGB as low-mass stars evolve onto the horizontal branch or red clump [25, 48]. The following subsections detail all aspects of measuring the TRGB, including an overview of existing methods, and a revisiting of the fundamentals of locating a discontinuity or edge in a dataset. We further summarize the simple yet robust approach to measuring the TRGB for the high signal-to-noise targets adopted by the CCHP. We then describe artificial star tests that inform us how to optimize the measurement of the TRGB such that we minimize the statistical and systematic uncertainties associated with our method. Finally, we present our estimates of the four TRGBs as part of this study and compute their true distance moduli based on a provisional estimate of the I-band TRGB luminosity.

3.2 Edge Detection Methodology

An early approach to measuring the TRGB was to record the magnitude of the brightest RGB stars, often located by simple binning of the LF [43, 42, 15, among others]. An arrow in Figure 2.3d demonstrates how the IC 1613 TRGB is prominent enough to be estimated by eye or ruler to within a few hundredths of a magnitude. This method was satisfactory when other sources of uncertainty, like the tip luminosity, dominated the error budget.

One of the first algorithmic approaches began with [30]. A review of the recent developments to the TRGB edge-detection is given in [21] and [26]. In summary, there are two fundamental approaches to measuring the TRGB. One applies a kernel to measure the point of greatest change in the LF as the TRGB, typically binning and smoothing the data in some fashion. The second employs a maximum likelihood function to fit two slopes to the

luminosity function, one brighter than the TRGB that corresponds to foreground or AGB stars, and one fainter that is part of the RGB. The transition point between the two slopes marks the TRGB.

As described in [21], each approach has their own advantages and disadvantages. The methodology adopted in this study seeks a middle ground where the nature of the true slope of the LF is not as critical to the measurement itself. We further avoid issues of granularity with binning of the LF that have limited the precision of previous studies. First, the LF is finely binned such that stars are mostly isolated in their respective bins. The GLOESS (Gaussian-windowed, Locally-Weighted Scatterplot Smoothing) function is then applied to smooth out the inherent granularity of the incomplete LF. GLOESS is the preferred method of smoothing because the weighting function spans the entire dataset range. This feature is well-suited for suppressing noise brighter than the TRGB and therefore minimizing the chance of obtaining a false measurement.

Finally, a $[-1, 0, +1]$ kernel, which is the finite-differences approximation of the first-derivative, is run over the LF to detect the point of greatest change. This approach was shown to be indistinguishable from existing methods in [21] for the ideal case of the bright and isolated TRGB for IC 1613.

3.3 Edge Detector Optimization

In the measurement of the TRGB, we seek the value of the GLOESS smoothing scale that would minimize the combination of statistical and systematic errors for our edge detection kernel. To understand an approach that would adequately assess these properties, we looked to existing literature on edge detection. A prominent area of edge image is digital image processing. The transition between the highs and lows of an image is not dissimilar to the transition seen in a galaxy LF in that it can be a sharp, pixel-wide jump or simply blurred.

Although edge detection methods have long been applied in astrophysical contexts, the assessment of uncertainties associated with the TRGB measurement from a digital imaging

processing standpoint is presented for the first time in this work. In particular, in order to assess the performance of an edge detector (in terms of accuracy and precision), one must simulate the conditions under which the measurement is made. With a large ensemble of comparable measurements, one can then assess the performance.

In the case of the TRGB, there is one measurement despite that the fact that there are many stars that contribute to that measurement. In practice, one could make observations of different parts of a galaxy and assess the uncertainties in the measurement by how the TRGB changes under the same methodology. This approach is resource-expensive, however. The alternative is to generate artificial luminosity functions that mimic the real observations as closely as possible. Then, keeping the [-1,0,+1] kernel fixed, we model the effect of the GLOESS smoothing scale (henceforth often referred to as σ_s).

3.3.1 Artificial Star Luminosity Functions

In order to appropriately model the RGB and AGB populations for our observations and make an informed measurement of the TRGB for each galaxy, we first assumed the RGB LF had a slope of 0.3 dex mag^{-1}, which is well-constrained in both theoretical and observed LFs [65, 40]. This estimate for the slope of the RGB LF has also been widely confirmed in TRGB studies where the slope is treated as a free parameter [see e.g. 36, 10]. For the AGB population, some studies have assumed the LF slope to be flat [e.g. 13, 39]. Modeling observed populations, however, suggests that the AGB LF slope could be in the range 0.3±0.2 dex mag^{-1} [36]. We have assumed an the intermediate value of 0.1 dex mag^{-1}.

Stars were then sampled at random from these luminosity functions, ranging from 1 magnitude brighter than the anticipated TRGB to 1 magnitude fainter. These stars were placed into our frames at pixel coordinates chosen by randomly sampling from a uniform distribution in X and Y. Typically 1000 stars per iteration was sufficient to avoid introducing crowding effects. Stars were added to the 'master list' of sources and photometry was performed and calibrated as before. This process was repeated until a large sample size of

stars was generated, or at least 100 times the estimated number of stars within the CMDs. We refer to this final output as 'master' artificial star luminosity functions (ASLFs).

3.3.2 Simulating TRGB edge detections

To gain insight into our edge detector, as well as the optimal level of smoothing for each set of observations, we downsample the 'master' ASLF for each galaxy to match the approximate number of RGB and AGB stars to populate a single, smaller ASLF. This ASLF samples both the AGB and RGB populations, and the relative number of AGB stars sampled within 0.1 mag of the TRGB is normalized to be 20% of the total number to match the approximate greatest fraction that has been recently observed local galaxies [52].

Since the LF binning can be arbitrarily small, i.e. σ_s in GLOESS smoothing can simply be increased to compensate for additional noise in the LF, we choose a bin size 0.005 mag such that stars are mostly isolated in their bins and the computation time for GLOESS remains short. For a fixed σ_s, we first run GLOESS on the downsampled ASLF. We then suppress any remaining Poisson noise by assigning a signal-to-noise weight based on the number of stars in each bin as described in [21]. These weights transform the output of the response function for a given bin from any edge detector into a statistical quantity related to the number of standard deviations above a baseline signal.

We then run our edge detector kernel across the smoothed LF and record the location of maximum response. We repeat the sampling, smoothing, and edge detection process until the average measurement of the TRGB converges, typically 5000 iterations, for the fixed σ_s. The distribution of detected edges then reveals the systematic and statistical uncertainties associated with the chosen σ_s for our edge detector. We then adjusted σ_s and repeated the analysis. Where the combined average systematic offset and dispersion of estimates are minimized is set to be the optimal level of smoothing. A sample result for the study of IC 1613 is given in Figure 3.1, taken from [21].

We find generally that the simulated AGB component simulated has no substantial effect

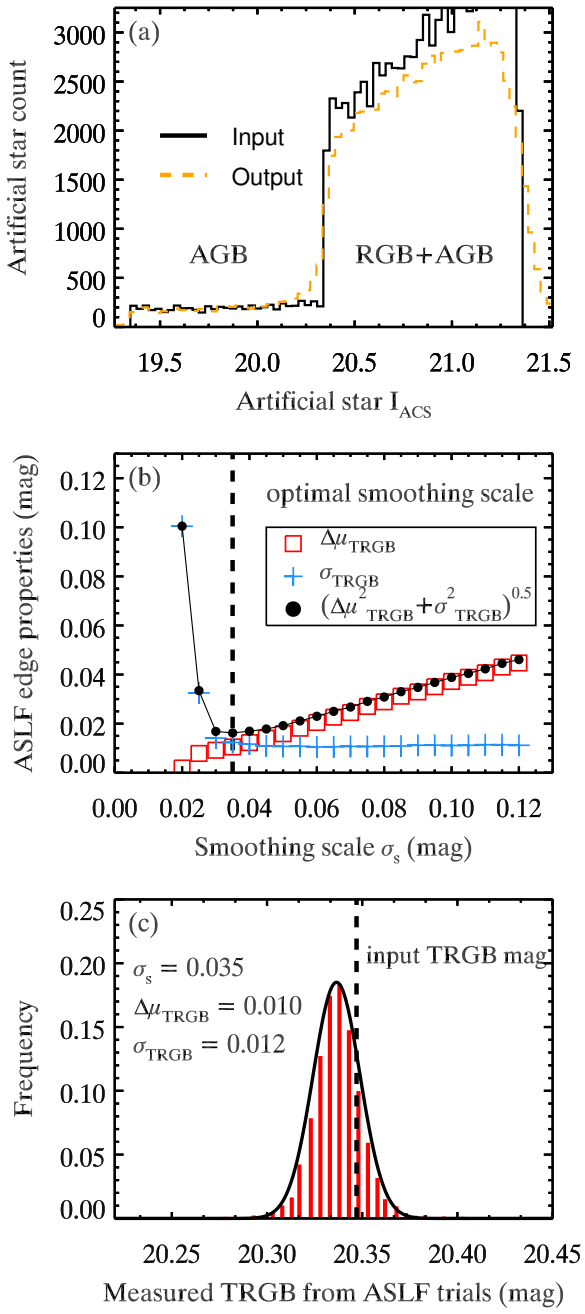

Figure 3.1: Artificial star tests of the luminosity function edge detection methodology for IC 1613

on the measured TRGB magnitudes. The ratio of TRGB to AGB stars near the tip is ∼4:1, which might, conceivably, cause a TRGB measurement to be systematically brighter. Nonetheless, we find that the signal-to-noise of the TRGB still outweighs the noise component due to AGB stars and there are minimal systematic effects.

3.4 Rectifying the Tip of the Red Giant Branch for Metallicity

As mentioned previously, the shape of the TRGB for each galaxy is a proxy for metallicity. In each of the galaxies in this work, the TRGB are broadly metal-poor, in part because of the targeting of galaxy halos. Generally, the color range in F606W-F814W (and $V-I$) is small enough (about 0.3-0.5 mag) that there is visually no metallicity effect. An analysis by [27] showed that the TRGB in ACS passbands, to which our observations are calibrated, can be rectified using a color-dependent quadratic formula called 'QT'. Applying their formulation to IC 1613, for example, a suitable magnitude correction to further flatten the TRGB in F606W and F814W is only +0.007 mag for F606W − F814W = 1.35, the approximate red end of the RGB (see Figure 2.3). The blue end of the TRGB corresponds to the most metal-poor component and therefore has an even smaller correction.

The apparent color-range for the Virgo Constellation galaxies is larger than that of IC 1613, but the typical error in color of TRGB stars exceeds 0.1 mag, indicating that they are plausibly as metal-poor as the IC 1613 sample. We conclude that the TRGB for each galaxy in this work does not require a metallicity correction.

3.5 Setting the Tip of the Red Giant Branch Distance Scale

Although it will be possible in the near future to directly calibrate the TRGB luminosity (see 6.1) using Milky Way RGB stars (discussed later), the current value of the I-band TRGB luminosity has been based on independently derived distances including eclipsing binaries, Cepheids, and RR Lyrae. The long-standing approximation in the literature, $M_I^{\rm TRGB} \approx$

-4 mag, is still consistent to within 1-σ of more recent estimates [39, 51].

Based on recent eclipsing binary distances to the LMC [45], as well as a recent calibration of the TRGB luminosity (Freedman et al. in prep) suggest a tip luminosity $M_I = -3.95 \pm 0.05$ mag, which is slightly fainter than, but still consistent with, the original estimate ≈ -4 mag. In the following, we therefore adopt a provisional tip luminosity $M_I = -3.95 \pm 0.05$ mag.

3.6 TRGB Measurements, Reddening, and Distances

We next consider the extent of foreground and internal extinction. For IC 1613, the [56] dust maps give a median color-excess per source from foreground extinction $E(B-V) \approx 0.025$ mag, which corresponds to $A_{\rm F814W} \approx 0.038$ mag assuming the [6] reddening law. For NGC 4424, NGC 4526, and NGC 4536, the estimated $E(B-V)$ do not exceed 0.02 mag. Given the large intrinsic scatter in estimated $E(B-V)$ of $\sigma_{BV} \approx 0.03$, we adopt the estimated reddening as a systematic uncertainty in our distance estimates. We apply the foreground extinction correction to the Virgo Constellation galaxies, but in the case of IC 1613, an independent case against reddening can be made, which we later revisit in the context of its RR Lyrae.

Any residual reddening would have to then arise from within the galaxies themselves. As mentioned in the introduction, internal reddening in IC 1613 has long been considered to be negligible based on the visibility of background galaxies through the main body of the galaxy itself. Furthermore, the specific targeting of galaxy halos for the remaining galaxies minimizes implies there is negligible internal reddening as well. For these reasons, we do not include a correction for internal reddening within the TRGB galaxies.

Figure 3.2 displays the TRGB edge detection for IC 1613. We find a TRGB magnitude $I = 20.35 \pm 0.01_{stat} \pm 0.01_{sys}$ mag. The results for NGC 4424, NGC 4526, and NGC 4536 are displayed in Figure 3.3. For these galaxies, we find extinction-corrected TRGB magnitudes 26.89 ± 0.05, 26.94 ± 0.05, and 26.98 ± 0.05 mag, respectively. The corresponding distance

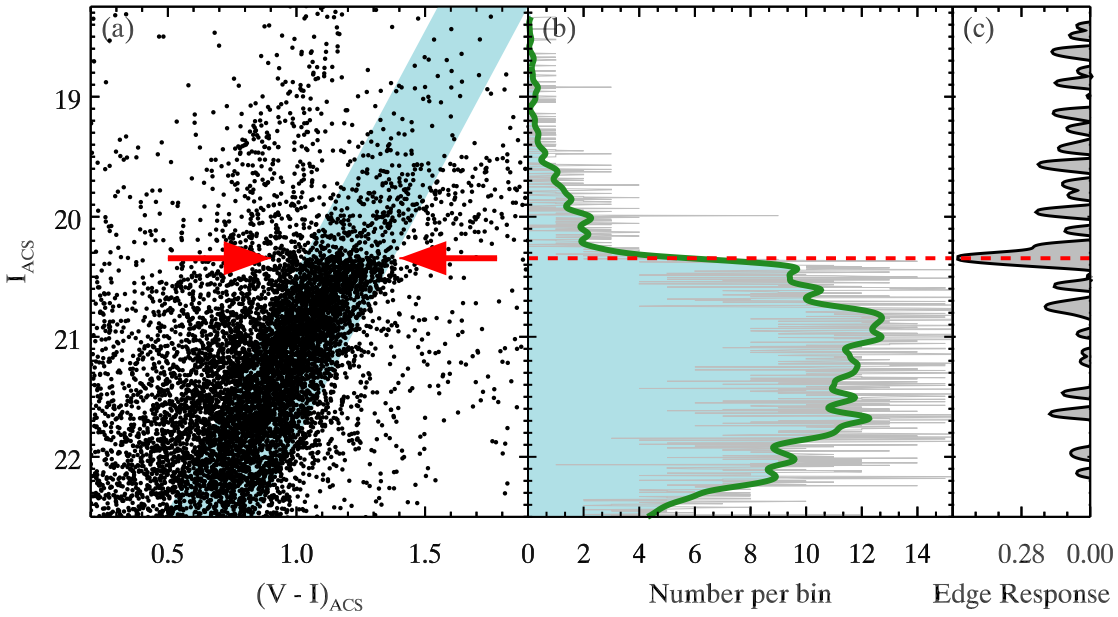

Figure 3.2: The IC 1613 TRGB edge detection

moduli are, in the order listed above, 24.30 ± 0.05, 30.84 ± 0.05, 30.79 ± 0.05, and 30.92 ± 0.05 mag.

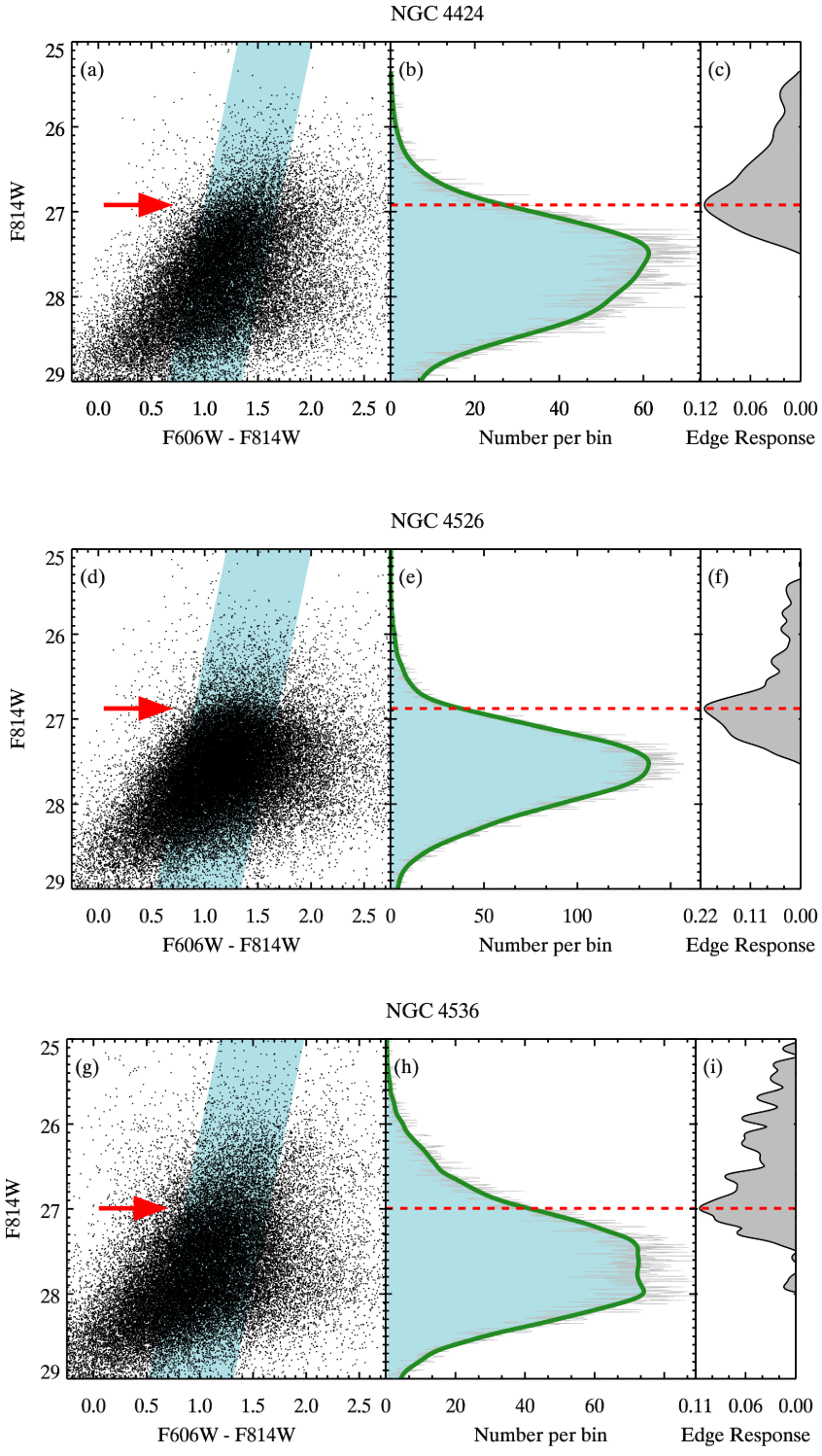

Figure 3.3: TRGB edge detection for NGC 4424, NGC 4526, and NGC 4536

CHAPTER 4

RR LYRAE AS A CHECK ON POP II DISTANCES

RRL are low-metallicty, He-burning stars with periods $0.2 \lesssim p \lesssim 1.1$ days. They are frequently used to estimate distances within the Milky Way [44, 60, for example], as well as nearby within the Local Group [53, 9, among many others]. Traditionally, RRL distances have been obtained from the V-band luminosity-metallicity relationship, though at longer wavelengths (such as the near-infrared), RRL follow period-luminosity relations [for a comprehensive introduction, see e.g. 62].

There are two primary sub-types of RRL: the RRab and the RRc. The RRab pulsate in the fundamental mode (FU), with a larger amplitude and asymmetric 'saw-tooth' light curve shape; and the RRc pulsate in the first-overtone mode (FO), with a smaller amplitude and a sinusoidal light curve shape. The physical mechanisms behind the radial pulsation of RR Lyrae are physically independent of the TRGB and are therefore an excellent internal test on the Pop II distance scale. Because RR Lyrae are typically several magnitudes fainter than the TRGB, the RR Lyrae analysis presented here applies to only IC 1613 where they are detectable in the current imaging.

4.1 The RRL sample

The RRL sample used in the study of IC 1613 was first cataloged by [4] and confirmed in [21] by their light curve morphology and placement in the Horizontal Branch of the CMD. There are 85 RRab and RRc within the archival imaging dataset, and 57 in the NIR imaging. Light curves and image cutouts for four RRab or RRc in our sample are shown in Figure 4.1. Column (a) shows the light curves in F475W (blue), F814W (red), and F160W (black). F160W light curves use the periods determined with the archival ACS/WFC photometry. The remaining columns (b), (c), and (d) are image cutouts of size $3.7'' \times 3.7''$ in the F475W, F814W, and F160W imaging, respectively. In each cutout, a circle identifies the RRL. The

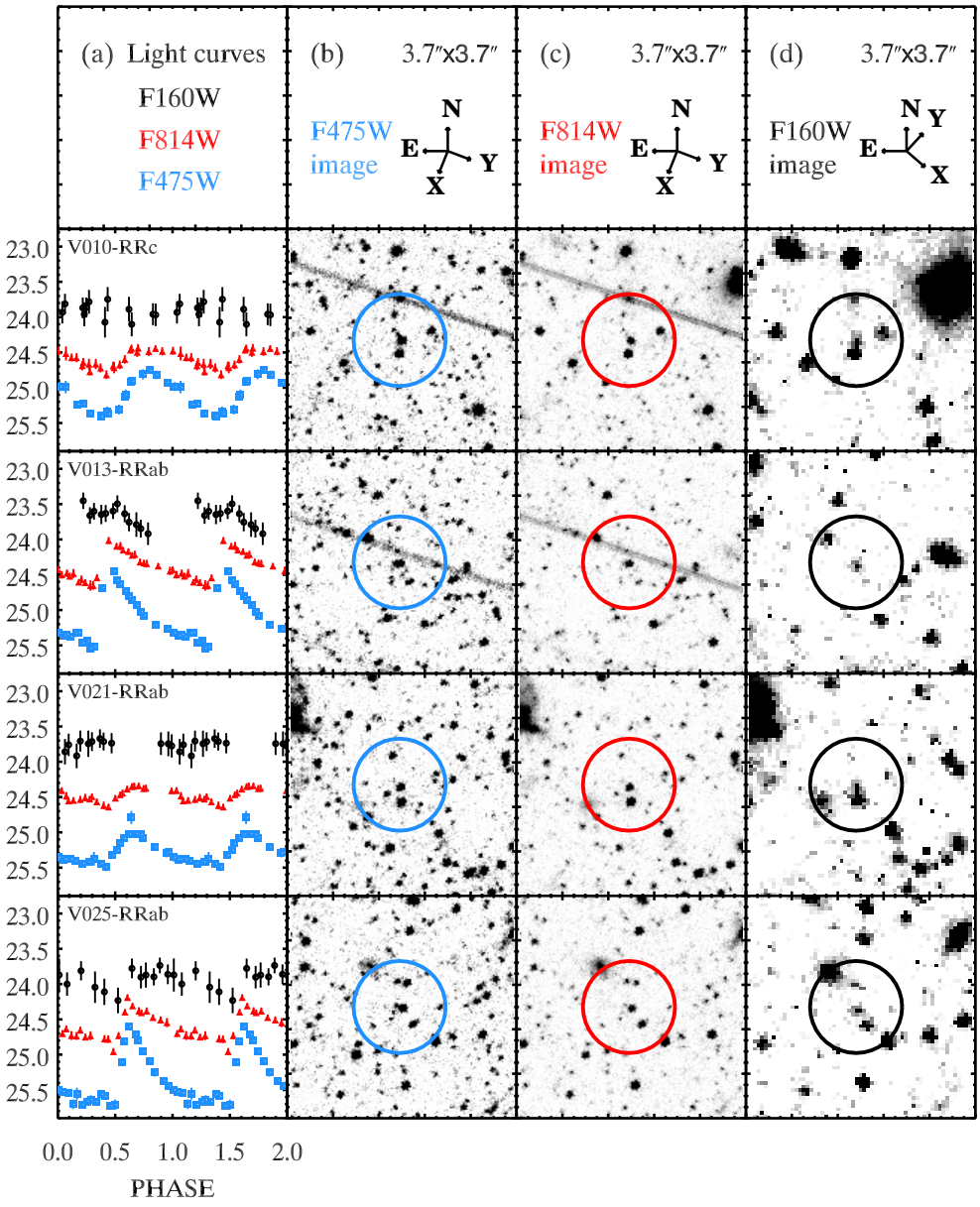

Figure 4.1: Sample IC 1613 RR Lyrae light curves

complete set of plots can be found in [21].

4.2 Mean Magnitudes

In the analysis that follows, the average magnitude for each RRL is computed as phase-averaged fluxes. Specifically, GLOESS-weighted fluxes are computed on a grid of 100 evenly-spaced phase points for each light curve using a 0.1 phase smoothing scale, which are averaged and reverted back to a magnitude. In many cases below, we refer to the ACS/WFC and WFC3/IR filters by their Johnson-Cousins counterparts, $BVIH$, except where noted in the discussion of transmission efficiencies.

Beyond average F475W, F814W and F160W magnitudes, we compute 4 additional magnitudes using a combination of these three ACS filters. First, we calculate V-magnitudes from F475W and F814W using the approximation $V \sim (\mathrm{F475W} + \mathrm{F814W})/2$ from [4], which flattens the Horizontal Branch. We further calculate Wesenheit magnitudes for each RRL, which use the total-to-selective absorption of two or three passbands in order to minimize the uncertainty in the reddening of observations [early use includes 32]. The Wesenheit magnitudes used here have the following forms:

$$\begin{aligned} W_{I,B-I} &= \mathrm{F814W} - 0.86\,(\mathrm{F475W} - \mathrm{F814W})\,, \\ W_{H,I-H} &= \mathrm{F160W} - 0.44\,(\mathrm{F814W} - \mathrm{F160W})\,, \\ W_{H,B-I} &= \mathrm{F160W} - 0.24\,(\mathrm{F475W} - \mathrm{F814W})\,. \end{aligned} \tag{4.1}$$

where we have adopted the Wesenheit labels from [37], and we have re-computed the above color-coefficients using the estimated reddening for the ACS filters (obtained via NED).

4.3 Period-Luminosity and Period-Wesenheit relations

Figure 4.2 contains the V-band and PL/PW relations used in this study, adopting the periods determined by [4]. Panels (a) and (b) show the average $BVIH$ magnitudes against

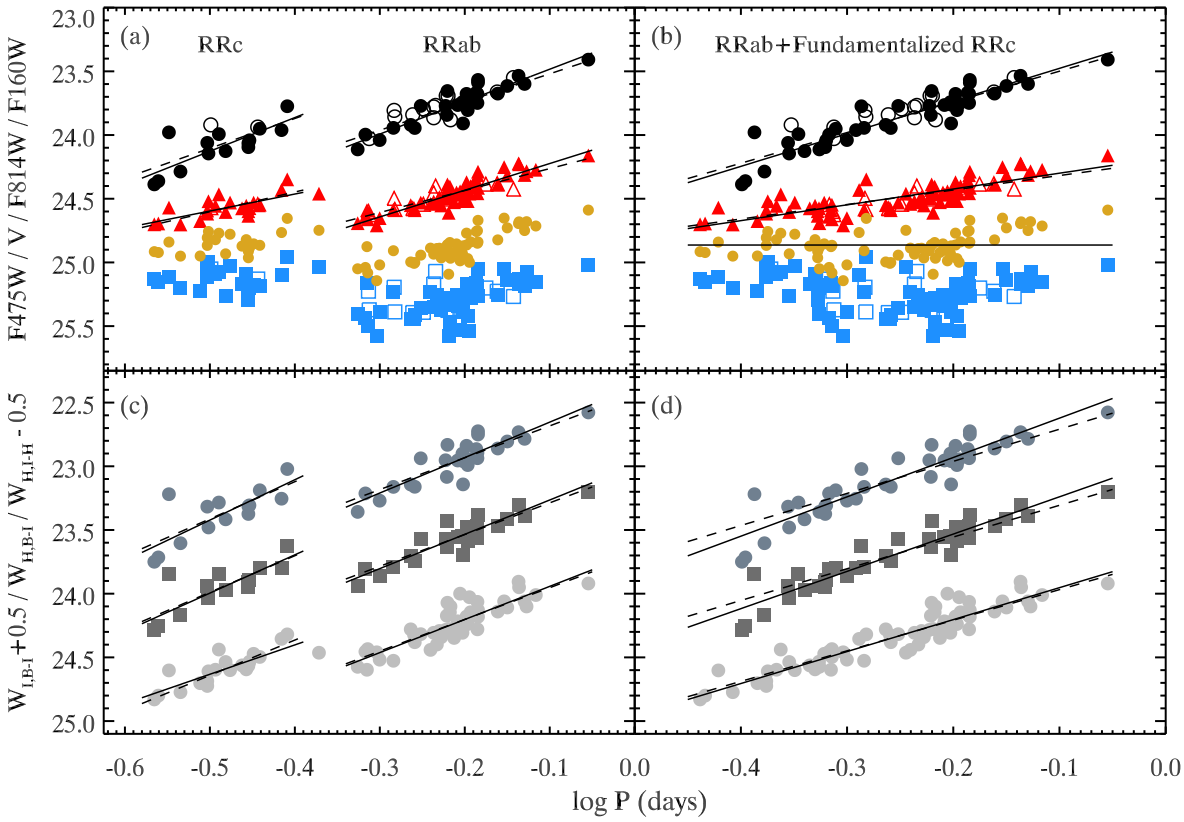

Figure 4.2: RR Lyrae PL relations for IC 1613

their periods, and panels (c) and (d) show the Wesenheit magnitudes defined above. In panels (a) and (b), open symbols denote RRL that have photometry that is possibly- or confirmed-blended. Details on the PL relations and slope fits are given in Table 3 of [21].

The location of the two primary types of RRL used in this study are labeled in panel (a) of Figure 4.2. All RRab observed in this study show a relationship between period and luminosity. However, in the case of F475W and V, fundamentalizing the RRc shows that there is no slope to the PL relations [see the theoretical discussion of this property in 7]. RRL in F814W, F160W, $W_{I,B-I}$, $W_{H,I-H}$, and $W_{H,B-I}$ all show PL/PW relations in their RRab, RRc, and fundamentalized forms.

Best-fit lines are shown in Figure 4.2 from three sources: fits to observations in this study are shown as solid lines; for panels (a) and (b), dashed lines use slopes obtained from the analysis of RRL in M 4; and for panels (c) and (d), dashed lines use the slopes of theoretical PWZ relations (period-Wesenheit-metallicity) from [37]. In all cases, there is agreement between the slopes determined independently from this study with both the M 4 empirical relations and the theoretical PWZ relations. There is virtually no difference in the quality of the fits despite the differing slopes. Generally, the fundamentalized F814W and F160W PL relations in panel (b) and the PWZ relations in panel (d) of Figure 4.2 show the least agreement by eye with the best-fit lines for IC 1613 observations. Nonetheless, the root-mean-square deviations for the empirical and theoretical fits show that the quality of the fits are also indistinguishable. For example, the $W_{H,I-H}$ fits have values 0.11 and 0.12 mag about the observed and theoretical best-fit lines, respectively.

4.4 RRL Zero-points

The zero-points used for the F814W and F160W PL relations are described in detail in [21]. We rely on the *HST* parallaxes of 5 Galactic RRL (4 RRab and 1 RRc). For the Wesenheit magnitudes (Figures 4.2c and 4.2d), we use theoretical PWZ relations and therefore compare the RRab and RRc results separately in addition to their fundamentalized forms. Photom-

etry used in establishing the zero-points is given in [41] and the general process is described in [2]. For the V-band magnitudes, we assume a mean IC 1613 RRL halo metallicity of [Fe/H] $= -1.2$ dex as measured directly using Fe lines by [28] at the radial location of the RRL sample. Via [9] we calculate that $M_V = +0.63 \pm 0.14$ mag, where we have adjusted their LMC distance assumption to 18.49 mag based on the result of [45].

4.5 RRL Distance to IC 1613

Several distances are obtainable using a combination of the different PL/PW and V-band relations. The results for individual relations are provided in [21]. We find that the current uncertainties in the RRL zero-points dominate the distance error budget, and we determine that (foreground) reddening is small enough for IC 1613 that it is consistent with zero. Combining the 9 RRL distances calculated above, we find a weighted-average distance modulus 24.28 ± 0.04 mag. For Pop II stars, there is therefore good agreement between TRGB and RR Lyrae distances to IC 1613. The observables, i.e. the measured TRGB and the RRL PL/PW relations, yield impressively consistent results at the 0.02 mag level.

CHAPTER 5

COMPARING POP I AND POP II DISTANCE SCALES

5.1 IC 1613: TRGB, RR Lyrae, and Cepheids

Individual estimates in Figure 5.1 show that there is considerable scatter in reported distance moduli for IC 1613, but generally there is a consistent picture when these determinations are brought onto a common system. Each weighted-average estimate and error on the mean show visually that the different distance indicators are consistent within their own class—Cepheid, RRL, or TRGB. It is also clear that RRL and recent Cepheid distances agree well, namely those of [18] and [58]. Recent updates to archival optical and infrared data such as [35], who found distance moduli 24.32 ± 0.04 and 24.24 ± 0.06 mag for VI and 3.6μm, respectively, also agree with the smaller distance modulus for IC 1613. [35] suggest that crowding could be the cause for the brighter observations (smaller distance moduli), but the agreement with the optical TRGB results presented here suggests that crowding for IC 1613 (at the very least in the optical) is not a critical issue. The outlier in recent Cepheid distances is that of [4], though as [58] showed, a metallicity correction to their W_I estimate brings their distance modulus to 24.33 ± 0.14 mag, i.e. in line with the other recent results.

We can quantitatively estimate the extent to which the average distances obtained from RRL and Cepheids differ. We calculated an unequal variances t-test on the adjusted collection of all RRL distances with the recent Cepheid sample. We obtained a p-value of 0.64 under the null hypothesis that they have the same mean. This result suggests that there is no compelling evidence that they belong to different distributions. This compilation of distances therefore suggests a close correspondence between Pop I and II distance indicators for IC 1613.

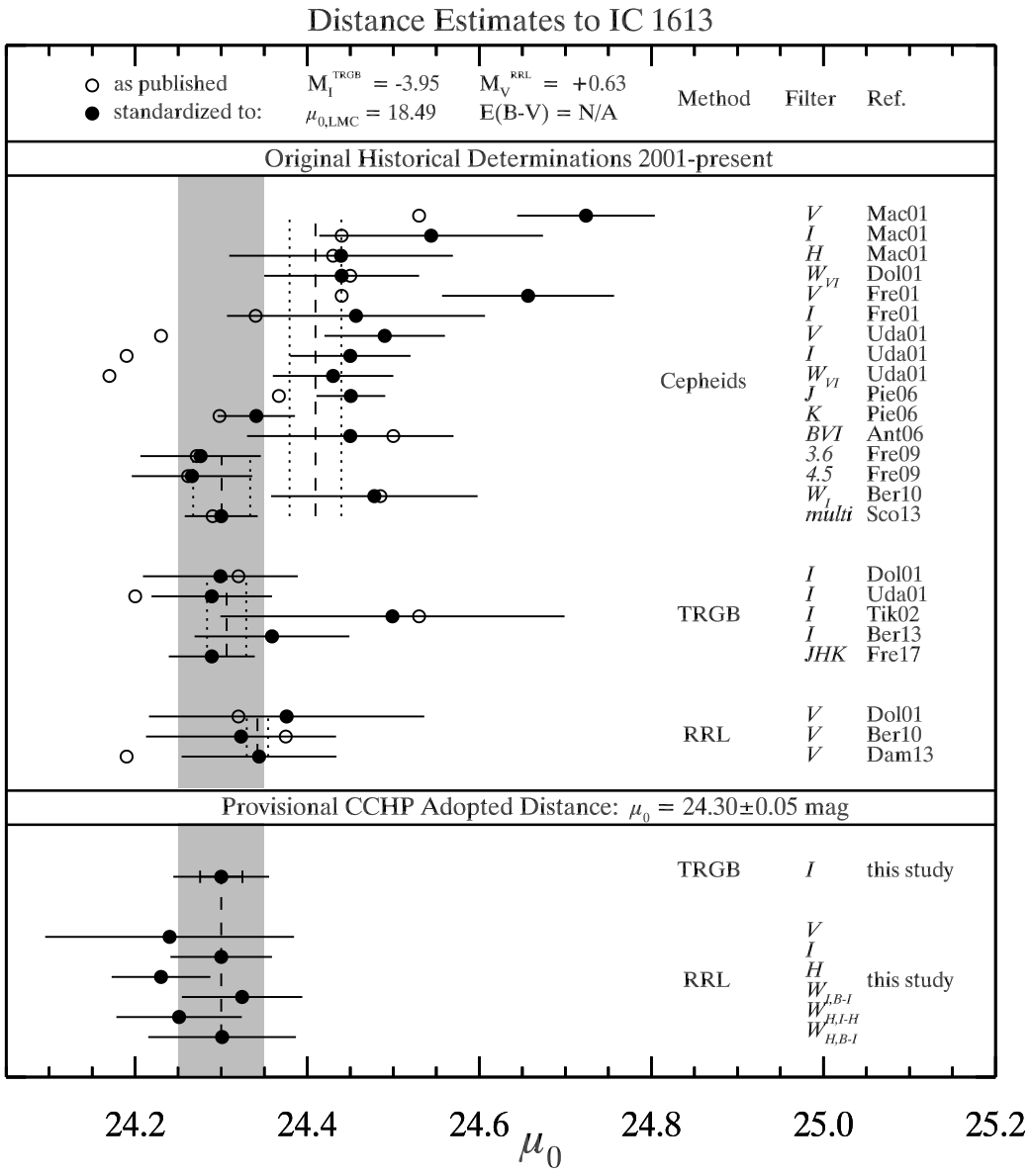

Figure 5.1: Distance estimates to IC 1613 since the Hubble Key Project.

5.2 NGC 4424 and NGC 4536 TRGB vs Cepheid Distances

There are currently 4 publications at the time of this writing that report a distance for NGC 4424. Two of these estimates are based on the Tully-Fisher relation, and one is based on observations of SN 2012cg itself, i.e. not independent for the objective of the CCHP. The fourth and most recent estimate is based on 3 Cepheids via [50]. The relatively small number of stars to construct the period-luminosity relations results in a distance 31.08 ± 0.29 mag. The distance determined here, 30.84, is consistent to within a single standard deviation of their estimated measurement uncertainties. This distance determined here is at the brighter end of the compilation of estimates, but it is also the most precise to date. The mean and median via NED are 30.96 ± 0.13 and 30.92 ± 0.14 mag, respectively, where the uncertainty on the median is the median-absolute-deviation scaled to a Gaussian standard deviation. These values are also consistent with the value determined here to within a single standard deviation.

NGC 4536 has the most distance estimates of the three galaxies considered in this study, owing to the fact that over 2 dozen Cepheids are known in this face-on spiral galaxy. The mean and median estimates are 30.85 ± 0.39 and 30.83 ± 0.21 mag, respectively, compared to 30.92 mag as determined here. Although the compilation of estimates spans a large range in distance, at the conclusion of the HST Key Project, the Cepheid-based distance modulus (with a metallicity correction) stood at 30.87 ± 0.04 mag [16], which is in agreement with what is determined here. The most re- cent Cepheid-based estimate at the time of this writing, 30.91 ± 0.05 mag via [50], is also in agreement with our estimate to well within a single standard deviation.

The agreement between TRGB and Cepheids distance presented here, representing a much greater distance than IC 1613, also indicates consistency between Pop I and II indicators.

CHAPTER 6

THE FUTURE OF THE TIP OF THE RED GIANT BRANCH

6.1 Direct Calibration of the Tip of the Red Giant Branch

The calibration of the TRGB presented above relies on the distances to the LMC. Although this distance is relatively well constrained by detached eclipsing binary stars, future results will present the opportunity for a direct calibration of the TRGB.

The *Gaia* project has released its initial catalog of parallax, named the Tycho-Gaia Astrometric Release [31, TGAS], but will present its own internal, *Gaia*-exclusive release in 2018. The CCHP is currently observing Milky Way RGB stars using the *TMMT* telescope at Las Campanas [41], which, with accurate parallaxes, will allow for the construction of the Milky Way TRGB luminosity. The uncertainty associated with the observations of RGB stars is statistical, and therefore the only systematic uncertainty in determining the zero-point will be from parallax—a value that is predicted to be vanishingly small.

6.2 The Near-Infrared Tip of the Red Giant Branch

As described above, observations in the NIR are often preferred because of the reduced effect of foreground and internal reddening. Existing tools like the *HST* WFC3/IR camera have been used to study the TRGB, but in the near future *James Webb Space Telescope* (*JWST*) has the potential to surpass the current limits of the NIR TRGB and extend much further in distance, thereby expanding the number of possible SNe Ia hosts. In particular, *JWST* has a primary aperture (6.5 m) that is more than double the size of *HST* (2.4 m). In the NIR, *JWST* should attain comparable resolution to *HST* in the optical.

CHAPTER 7

CONCLUSION

We have resolved the TRGB of four galaxies: IC 1613, NGC 4424, NGC 4526, and NGC 4536. We have further made comparisons to existing Cepheid and RR Lyrae-based distances where available. The distances presented here are some of the most high-fidelity to date and are set to improve with anchoring of the TRGB luminosity through *Gaia*-based parallaxes. We have found good agreement between TRGB and Cepheid distances, spanning $\sim$ 730 kpc to $\sim$ 15 Mpc, which suggests a close correspondence between distances derived from stars of Pop I and II on a galaxy-by-galaxy basis. We expect that these and forthcoming results on the TRGB through the CCHP will provide a fresh look at Pop II stars as local and extragalactic distance indicators.

REFERENCES

[1] M. K. Barker, A. Sarajedini, and J. Harris. Variations in Star Formation History and the Red Giant Branch Tip. ApJ, 606:869–893, May 2004.

[2] R. L. Beaton, W. L. Freedman, B. F. Madore, G. Bono, E. K. Carlson, G. Clementini, M. J. Durbin, A. Garofalo, D. Hatt, I. S. Jang, J. A. Kollmeier, M. G. Lee, A. J. Monson, J. A. Rich, V. Scowcroft, M. Seibert, L. Sturch, and S.-C. Yang. The Carnegie-Chicago Hubble Program. I. An Independent Approach to the Extragalactic Distance Scale Using Only Population II Distance Indicators. ApJ, 832:210, December 2016.

[3] J. L. Bernal, L. Verde, and A. G. Riess. The trouble with H_0. J. Cosmology Astropart. Phys., 10:019, October 2016.

[4] E. J. Bernard, M. Monelli, C. Gallart, A. Aparicio, S. Cassisi, I. Drozdovsky, S. L. Hidalgo, E. D. Skillman, and P. B. Stetson. The ACS LCID Project. II. Faint Variable Stars in the Isolated Dwarf Irregular Galaxy IC 1613. ApJ, 712:1259–1276, April 2010.

[5] G. Bono, F. Caputo, M. Marconi, and I. Musella. Insights into the Cepheid Distance Scale. ApJ, 715:277–291, May 2010.

[6] J. A. Cardelli, G. C. Clayton, and J. S. Mathis. The relationship between infrared, optical, and ultraviolet extinction. ApJ, 345:245–256, October 1989.

[7] M. Catelan, B. J. Pritzl, and H. A. Smith. The RR Lyrae Period-Luminosity Relation. I. Theoretical Calibration. ApJS, 154:633–649, October 2004.

[8] Márcio Catelan and Horace A. Smith. *Pulsating Stars*. Wiley-VCH, 1 edition, 2015.

[9] G. Clementini, R. Gratton, A. Bragaglia, E. Carretta, L. Di Fabrizio, and M. Maio. Distance to the Large Magellanic Cloud: The RR Lyrae Stars. AJ, 125:1309–1329, March 2003.

[10] A. R. Conn, R. A. Ibata, G. F. Lewis, Q. A. Parker, D. B. Zucker, N. F. Martin, A. W. McConnachie, M. J. Irwin, N. Tanvir, M. A. Fardal, A. M. N. Ferguson, S. C. Chapman, and D. Valls-Gabaud. A Bayesian Approach to Locating the Red Giant Branch Tip Magnitude. II. Distances to the Satellites of M31. ApJ, 758:11, October 2012.

[11] G. S. Da Costa and T. E. Armandroff. Standard globular cluster giant branches in the ($M_{I,/V-I/sub}$ O) plane. AJ, 100:162–181, July 1990.

[12] A. Dressler, B. Bigelow, T. Hare, B. Sutin, I. Thompson, G. Burley, H. Epps, A. Oemler, A. Bagish, C. Birk, K. Clardy, S. Gunnels, D. Kelson, S. Shectman, and D. Osip. IMACS: The Inamori-Magellan Areal Camera and Spectrograph on Magellan-Baade. PASP, 123:288–332, March 2011.

[13] P. R. Durrell, R. Ciardullo, J. J. Feldmeier, G. H. Jacoby, and S. Sigurdsson. Intracluster Red Giant Stars in the Virgo Cluster. ApJ, 570:119–131, May 2002.

[14] W. Freedman. CHP-II: The Carnegie Hubble Program to Measure Ho to 3% Using Population II. HST Proposal, October 2014.

[15] W. L. Freedman. Stellar content of nearby galaxies. I - BVRI CCD photometry for IC 1613. AJ, 96:1248–1306, October 1988.

[16] W. L. Freedman, B. F. Madore, B. K. Gibson, L. Ferrarese, D. D. Kelson, S. Sakai, J. R. Mould, R. C. Kennicutt, Jr., H. C. Ford, J. A. Graham, J. P. Huchra, S. M. G. Hughes, G. D. Illingworth, L. M. Macri, and P. B. Stetson. Final Results from the Hubble Space Telescope Key Project to Measure the Hubble Constant. ApJ, 553:47–72, May 2001.

[17] W. L. Freedman, B. F. Madore, V. Scowcroft, C. Burns, A. Monson, S. E. Persson, M. Seibert, and J. Rigby. Carnegie Hubble Program: A Mid-infrared Calibration of the Hubble Constant. ApJ, 758:24, October 2012.

[18] W. L. Freedman, J. Rigby, B. F. Madore, S. E. Persson, L. Sturch, and V. Mager. The Cepheid Period-Luminosity Relation (The Leavitt Law) at Mid-Infrared Wavelengths. IV. Cepheids in IC 1613. ApJ, 695:996–998, April 2009.

[19] C. Gallart. The Onset of Star Formation in the Universe: Constraints from Nearby Isolated Dwarf Galaxies. HST Proposal, July 2005.

[20] Harm J. Habing and Hans Olofsson. *Asymptotic Giant Branch Stars*. Springer, 2004.

[21] D. Hatt, R. L. Beaton, W. L. Freedman, B. F. Madore, I. S. Jang, T. J. Hoyt, M. G. Lee, A. J. Monson, J. A. Rich, V. Scowcroft, and M. Seibert. The Carnegie-Chicago Hubble Program. II. The Distance to IC 1613: The Tip of the Red Giant Branch and RR Lyrae Period-Luminosity Relations. *ArXiv e-prints*, March 2017.

[22] J. R. Herrnstein, J. M. Moran, L. J. Greenhill, P. J. Diamond, M. Inoue, N. Nakai, M. Miyoshi, C. Henkel, and A. Riess. A geometric distance to the galaxy NGC4258 from orbital motions in a nuclear gas disk. Nature, 400:539–541, August 1999.

[23] R. W. Hilditch, I. D. Howarth, and T. J. Harries. Forty eclipsing binaries in the Small Magellanic Cloud: fundamental parameters and Cloud distance. MNRAS, 357:304–324, February 2005.

[24] E. M. L. Humphreys, M. J. Reid, J. M. Moran, L. J. Greenhill, and A. L. Argon. Toward a New Geometric Distance to the Active Galaxy NGC 4258. III. Final Results and the Hubble Constant. ApJ, 775:13, September 2013.

[25] I. Iben, Jr. and A. Renzini. Asymptotic giant branch evolution and beyond. ARA&A, 21:271–342, 1983.

[26] I. S. Jang, D. Hatt, R. L. Beaton, M. G. Lee, W. L. Freedman, B. F. Madore, T. J. Hoyt, A. J. Monson, J. A. Rich, V. Scowcroft, and M. Seibert. The Carnegie-Chicago Hubble Program. III. The Distance to NGC 1365 via the Tip of the Red Giant Branch. *ArXiv e-prints*, March 2017.

[27] I. S. Jang and M. G. Lee. The Tip of the Red Giant Branch Distances to Type Ia Supernova Host Galaxies. IV. Color Dependence and Zero-point Calibration. ApJ, 835:28, January 2017.

[28] E. N. Kirby, J. G. Cohen, P. Guhathakurta, L. Cheng, J. S. Bullock, and A. Gallazzi. The Universal Stellar Mass-Stellar Metallicity Relation for Dwarf Galaxies. ApJ, 779:102, December 2013.

[29] E. Komatsu, K. M. Smith, J. Dunkley, C. L. Bennett, B. Gold, G. Hinshaw, N. Jarosik, D. Larson, M. R. Nolta, L. Page, D. N. Spergel, M. Halpern, R. S. Hill, A. Kogut, M. Limon, S. S. Meyer, N. Odegard, G. S. Tucker, J. L. Weiland, E. Wollack, and E. L. Wright. Seven-year Wilkinson Microwave Anisotropy Probe (WMAP) Observations: Cosmological Interpretation. ApJS, 192:18, February 2011.

[30] M. G. Lee, W. L. Freedman, and B. F. Madore. The Tip of the Red Giant Branch as a Distance Indicator for Resolved Galaxies. ApJ, 417:553, November 1993.

[31] L. Lindegren, U. Lammers, U. Bastian, J. Hernández, S. Klioner, D. Hobbs, A. Bombrun, D. Michalik, M. Ramos-Lerate, A. Butkevich, G. Comoretto, E. Joliet, B. Holl, A. Hutton, P. Parsons, H. Steidelmüller, U. Abbas, M. Altmann, A. Andrei, S. Anton, N. Bach, C. Barache, U. Becciani, J. Berthier, L. Bianchi, M. Biermann, S. Bouquillon, G. Bourda, T. Brüsemeister, B. Bucciarelli, D. Busonero, T. Carlucci, J. Castañeda, P. Charlot, M. Clotet, M. Crosta, M. Davidson, F. de Felice, R. Drimmel, C. Fabricius, A. Fienga, F. Figueras, E. Fraile, M. Gai, N. Garralda, R. Geyer, J. J. González-Vidal, R. Guerra, N. C. Hambly, M. Hauser, S. Jordan, M. G. Lattanzi, H. Lenhardt, S. Liao, W. Löffler, P. J. McMillan, F. Mignard, A. Mora, R. Morbidelli, J. Portell, A. Riva, M. Sarasso, I. Serraller, H. Siddiqui, R. Smart, A. Spagna, U. Stampa, I. Steele, F. Taris, J. Torra, W. van Reeven, A. Vecchiato, S. Zschocke, J. de Bruijne, G. Gracia, F. Raison, T. Lister, J. Marchant, R. Messineo, M. Soffel, J. Osorio, A. de Torres, and W. O'Mullane. Gaia Data Release 1. Astrometry: one billion positions, two million proper motions and parallaxes. A&A, 595:A4, November 2016.

[32] B. F. Madore. The period-luminosity relation. IV - Intrinsic relations and reddenings for the Large Magellanic Cloud Cepheids. ApJ, 253:575–579, February 1982.

[33] B. F. Madore, V. Mager, and W. L. Freedman. Sharpening the Tip of the Red Giant Branch. ApJ, 690:389–393, January 2009.

[34] V. A. Mager, B. F. Madore, and W. L. Freedman. The Metallicity Dependence of the Cepheid P - L Relation in M101. ApJ, 777:79, November 2013.

[35] D. Majaess, D. G. Turner, W. Gieren, and C. Ngeow. Evidence for photometric contamination in key observations of Cepheids in the benchmark galaxy IC 1613. A&A, 572:A64, December 2014.

[36] D. Makarov, L. Makarova, L. Rizzi, R. B. Tully, A. E. Dolphin, S. Sakai, and E. J. Shaya. Tip of the Red Giant Branch Distances. I. Optimization of a Maximum Likelihood Algorithm. AJ, 132:2729–2742, December 2006.

[37] M. Marconi, G. Coppola, G. Bono, V. Braga, A. Pietrinferni, R. Buonanno, M. Castellani, I. Musella, V. Ripepi, and R. F. Stellingwerf. On a New Theoretical Framework for RR Lyrae Stars. I. The Metallicity Dependence. ApJ, 808:50, July 2015.

[38] A. W. McConnachie. The Observed Properties of Dwarf Galaxies in and around the Local Group. AJ, 144:4, July 2012.

[39] A. W. McConnachie, M. J. Irwin, A. M. N. Ferguson, R. A. Ibata, G. F. Lewis, and N. Tanvir. Determining the location of the tip of the red giant branch in old stellar populations: M33, Andromeda I and II. MNRAS, 350:243–252, May 2004.

[40] B. Méndez, M. Davis, J. Moustakas, J. Newman, B. F. Madore, and W. L. Freedman. Deviations from the Local Hubble Flow. I. The Tip of the Red Giant Branch as a Distance Indicator. AJ, 124:213–233, July 2002.

[41] A. J. Monson, R. L. Beaton, V. Scowcroft, W. L. Freedman, B. F. Madore, J. A. Rich, M. Seibert, J. A. Kollmeier, and G. Clementini. Standard Galactic Field RR Lyrae. I. Optical to Mid-infrared Phased Photometry. AJ, 153:96, March 2017.

[42] J. Mould and J. Kristian. The stellar population in the halos of M31 and M33. ApJ, 305:591–599, June 1986.

[43] J. R. Mould, J. Kristian, and G. S. Da Costa. Stellar populations in local group dwarf elliptical galaxies. I - NGC 147. ApJ, 270:471–484, July 1983.

[44] J. H. Oort and L. Plaut. The distance to the galactic centre derived from RR Lyrae variables, the distribution of these variables in the galaxy's inner region and halo, and a rediscussion of the galactic rotation constants. A&A, 41:71–86, June 1975.

[45] G. Pietrzyński, D. Graczyk, W. Gieren, I. B. Thompson, B. Pilecki, A. Udalski, I. Soszyński, S. Kozłowski, P. Konorski, K. Suchomska, G. Bono, P. G. P. Moroni, S. Villanova, N. Nardetto, F. Bresolin, R. P. Kudritzki, J. Storm, A. Gallenne, R. Smolec, D. Minniti, M. Kubiak, M. K. Szymański, R. Poleski, Ł. Wyrzykowski, K. Ulaczyk, P. Pietrukowicz, M. Górski, and P. Karczmarek. An eclipsing-binary distance to the Large Magellanic Cloud accurate to two per cent. Nature, 495:76–79, March 2013.

[46] Planck Collaboration, P. A. R. Ade, N. Aghanim, C. Armitage-Caplan, M. Arnaud, M. Ashdown, F. Atrio-Barandela, J. Aumont, C. Baccigalupi, A. J. Banday, and et al. Planck 2013 results. XVI. Cosmological parameters. A&A, 571:A16, November 2014.

[47] Planck Collaboration, P. A. R. Ade, N. Aghanim, M. Arnaud, M. Ashdown, J. Aumont, C. Baccigalupi, A. J. Banday, R. B. Barreiro, J. G. Bartlett, and et al. Planck 2015 results. XIII. Cosmological parameters. *ArXiv e-prints*, February 2015.

[48] A. Renzini, L. Greggio, C. Ritossa, and L. Ferrario. Why stars inflate to and deflate from red giant dimensions. ApJ, 400:280–303, November 1992.

[49] I. Ribas, C. Jordi, F. Vilardell, E. L. Fitzpatrick, R. W. Hilditch, and E. F. Guinan. First Determination of the Distance and Fundamental Properties of an Eclipsing Binary in the Andromeda Galaxy. ApJ, 635:L37–L40, December 2005.

[50] A. G. Riess, L. M. Macri, S. L. Hoffmann, D. Scolnic, S. Casertano, A. V. Filippenko, B. E. Tucker, M. J. Reid, D. O. Jones, J. M. Silverman, R. Chornock, P. Challis, W. Yuan, P. J. Brown, and R. J. Foley. A 2.4% Determination of the Local Value of the Hubble Constant. ApJ, 826:56, July 2016.

[51] L. Rizzi, R. B. Tully, D. Makarov, L. Makarova, A. E. Dolphin, S. Sakai, and E. J. Shaya. Tip of the Red Giant Branch Distances. II. Zero-Point Calibration. ApJ, 661:815–829, June 2007.

[52] P. Rosenfield, P. Marigo, L. Girardi, J. J. Dalcanton, A. Bressan, M. Gullieuszik, D. Weisz, B. F. Williams, A. Dolphin, and B. Aringer. Evolution of Thermally Pulsing Asymptotic Giant Branch Stars. IV. Constraining Mass loss and Lifetimes of Low Mass, Low Metallicity AGB Stars. ApJ, 790:22, July 2014.

[53] A. Saha, W. L. Freedman, J. G. Hoessel, and A. E. Mossman. RR Lyrae stars in Local Group galaxies. IV - IC 1613. AJ, 104:1072–1085, September 1992.

[54] Maurizio Salaris and Santi Cassisi. *Evolution of Stars and Stellar Populations*. Wiley, 1 edition, 2005.

[55] A. Sandage. The Distance of the Local-Group Galaxy IC 1613 Obtained from Baade's Work on its Stellar Content. ApJ, 166:13, May 1971.

[56] E. F. Schlafly and D. P. Finkbeiner. Measuring Reddening with Sloan Digital Sky Survey Stellar Spectra and Recalibrating SFD. ApJ, 737:103, August 2011.

[57] D. J. Schlegel, D. P. Finkbeiner, and M. Davis. Maps of Dust Infrared Emission for Use in Estimation of Reddening and Cosmic Microwave Background Radiation Foregrounds. ApJ, 500:525–553, June 1998.

[58] V. Scowcroft, W. L. Freedman, B. F. Madore, A. J. Monson, S. E. Persson, M. Seibert, J. R. Rigby, and J. Melbourne. The Carnegie Hubble Program: The Infrared Leavitt Law in IC 1613. ApJ, 773:106, August 2013.

[59] V. Scowcroft, M. Seibert, W. L. Freedman, R. L. Beaton, B. F. Madore, A. J. Monson, J. A. Rich, and J. R. Rigby. The Carnegie Chicago Hubble Program: the mid-infrared colours of Cepheids and the effect of metallicity on the CO band-head at 4.6 μm. MNRAS, 459:1170–1178, June 2016.

[60] B. Sesar, Ž. Ivezić, R. H. Lupton, M. Jurić, J. E. Gunn, G. R. Knapp, N. DeLee, J. A. Smith, G. Miknaitis, H. Lin, D. Tucker, M. Doi, M. Tanaka, M. Fukugita, J. Holtzman, S. Kent, B. Yanny, D. Schlegel, D. Finkbeiner, N. Padmanabhan, C. M. Rockosi, N. Bond, B. Lee, C. Stoughton, S. Jester, H. Harris, P. Harding, J. Brinkmann, D. P. Schneider, D. York, M. W. Richmond, and D. Vanden Berk. Exploring the Variable Sky with the Sloan Digital Sky Survey. AJ, 134:2236–2251, December 2007.

[61] E. D. Skillman, S. L. Hidalgo, D. R. Weisz, M. Monelli, C. Gallart, A. Aparicio, E. J. Bernard, M. Boylan-Kolchin, S. Cassisi, A. A. Cole, A. E. Dolphin, H. C. Ferguson, L. Mayer, J. F. Navarro, P. B. Stetson, and E. Tolstoy. The ACS LCID Project. X. The Star Formation History of IC 1613: Revisiting the Over-cooling Problem. ApJ, 786:44, May 2014.

[62] Horace A. Smith. *RR Lyrae Stars*. Cambridge University Press, 1995.

[63] I. Soszyński, A. Udalski, M. K. Szymański, D. Skowron, G. Pietrzyński, R. Poleski, P. Pietrukowicz, J. Skowron, P. Mróz, S. Kozłowski, Ł. Wyrzykowski, K. Ulaczyk, and M. Pawlak. The OGLE Collection of Variable Stars. Classical Cepheids in the Magellanic System. Acta Astron., 65:297–312, December 2015.

[64] F. Vilardell, I. Ribas, C. Jordi, E. L. Fitzpatrick, and E. F. Guinan. The distance to the Andromeda galaxy from eclipsing binaries. A&A, 509:A70, January 2010.

[65] M. Zoccali and G. Piotto. Comparison between observed and theoretical Red Giant Branch luminosity functions of galactic globular clusters. A&A, 358:943–955, June 2000.